INTERNATIONAL JOURNAL FOR NUMERICAL METHODS IN ENGINEERING
Int. J. Numer. Meth. Engng 2008; **76**:1645–1677
Published online 22 July 2008 in Wiley InterScience (www.interscience.wiley.com). DOI: 10.1002/nme.2373

On computing the forces from the noisy displacement data of an elastic body

A. Narayana Reddy and G. K. Ananthasuresh*, †

Department of Mechanical Engineering, Indian Institute of Science, Bangalore, Karnataka, India

SUMMARY

This study is concerned with the accurate computation of the unknown forces applied on the boundary of an elastic body using its measured displacement data with noise. Vision-based minimally intrusive force-sensing using elastically deformable grasping tools is the motivation for undertaking this problem. Since this problem involves incomplete and inconsistent displacement/force of an elastic body, it leads to an ill-posed problem known as Cauchy's problem in elasticity. Vision-based displacement measurement necessitates large displacements of the elastic body for reasonable accuracy. Therefore, we use geometrically non-linear modelling of the elastic body, which was not considered by others who attempted to solve Cauchy's elasticity problem before. We present two methods to solve the problem. The first method uses the pseudo-inverse of an over-constrained system of equations. This method is shown to be not effective when the noise in the measured displacement data is high. We attribute this to the appearance of spurious forces at regions where there should not be any forces. The second method focuses on minimizing the spurious forces by varying the measured displacements within the known accuracy of the measurement technique. Both continuum and frame elements are used in the finite element modelling of the elastic bodies considered in the numerical examples. The performance of the two methods is compared using seven numerical examples, all of which show that the second method estimates the forces with an error that is not more than the noise in the measured displacements. An experiment was also conducted to demonstrate the effectiveness of the second method in accurately estimating the applied forces.

Received 19 October 2007; Revised 14 February 2008; Accepted 27 March 2008

KEY WORDS: vision-based force sensor; geometric non-linearity; inverse problems; Cauchy's problem

*Correspondence to: G. K. Ananthasuresh, Department of Mechanical Engineering, Indian Institute of Science, Bangalore, Karnataka, India.
†E-mail: suresh@mecheng.iisc.ernet.in

Contract/grant sponsor: Department of Science and Technology, Government of India

1. INTRODUCTION

This paper presents methods for the computation of forces acting on the boundary or the interior of a constrained elastic body using visually measured displacement data at selected points. The motivation for this problem is vision-based force-sensing in objects of small sizes using suitably designed and well-characterized grasping and manipulation tools that deform elastically (e.g. [1–3], see Figures 1(a) and (b)). Vision-based force-sensing is non-intrusive because neither does it involve any contact with the elastic body (other than the portions where the body is mechanically held) nor does it involve electric, magnetic, thermal, or other fields. In this technique, the images of the body are captured before, during, and after deformation using digital cameras and microscopy. Image processing helps in extracting the displacements from the visually captured images. Therefore, this method is popular in experimental mechanics where intrusive force-sensing techniques are to be avoided [4–6].

The method of computing forces is straightforward when sufficiently accurate displacement data are available at all points. However, two complications occur when the distances are known at only a few points or when the data are inaccurate. First, when distances are known at only a few points, additional information, such as stresses/strains at some points, the location(s) of the applied force(s), etc., is necessary for the accurate computation of forces. In vision-based force-sensing, the portions over which an object is in contact with other objects (i.e. the portions on which forces act) might be visually inaccessible for displacement measurement. For example, when a micromachined tool is grasping a biological cell, it would occlude the region of mechanical contact as shown in Figure 1(a). Hence, the location(s) of applied forces are known but neither force nor displacement is known at those locations. Second, the noise in the measured displacement data has a big influence on the accuracy of the computed force. The noise, which is inevitable in vision-based measurement, introduces large errors irrespective of whether the displacement data are given at all the points or at a few points and whether the locations of applied forces are known or not known [1].

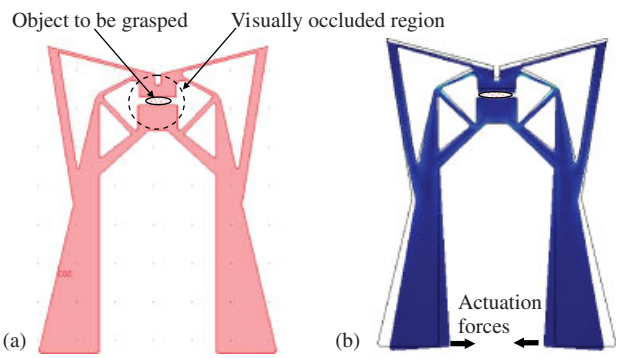

Figure 1. An object to be characterized held by an elastically deforming compliant gripper. By measuring the displacements of a few visually accessible points on the gripping tool, the forces acting on it by the actuator (which is not shown in the figure) and the object are computed using the methods presented in this paper. Note that the displacement of the gripper near the grasped object cannot be easily measured. Hence, the displacements of some other points (where there is no force) are measured. This leads to an inverse problem as explained in the text: (a) elastically deforming compliant gripper before applying forces and (b) after applying forces and grasping the object.

DOI: 10.1002/nme

These two features make the problem considered in this paper a reconstruction-type inverse problem [7]. This is in contrast with the parameter extraction-type inverse problem or identification of embedded entities (e.g. cracks, cavities, and inclusions) wherein the inhomogeneous material properties are estimated based on the measured displacements and forces [8].

In the reconstruction-type inverse problem in elasticity, the locations of applied forces and material properties of the elastic body are assumed to be known. Here, we estimate forces and displacements at inaccessible locations from measured displacements at a few locations. This is known as the Cauchy problem in elasticity [8, 7]. In particular, the focus of this paper is an inverse problem to the geometrically non-linear elastic boundary value problem.

In general, inverse problems are ill-posed in the sense that they do not satisfy one or more of the following: the existence of solution, uniqueness, or continuity/stability with respect to input information [9, 10]. The latter two are relevant for the problem considered in this paper. To see the non-uniqueness, consider a displacement-amplification compliant mechanism shown in Figures 2(a) and (b) [11]. The mechanism, which is an elastic body undergoing large deformation, is fixed at points C and D. Horizontal and vertical forces are applied at point A with different magnitudes in cases (a) and (b). Although the forces are different, in both cases the displacement at point B is the same. Clearly, the deformation patterns in the two load cases are very different. In fact, we found more load cases where point B can be made to displace by the same amount, but the deformation pattern is significantly different. This shows that if we measure displacement at only a few points (in the example of Figures 2(a) and (b), only at one point, B), the solution (i.e. the computed force) is not unique even though we have assumed the location of the force. Next, the lack of continuity in the computed forces with respect to measured displacement data can be seen in almost all the examples presented in the literature and in this paper (see Section 5). In other words, for small random perturbations in the displacement data, there is usually a large change in the computed forces. This can be understood as follows. Consider a deformed pattern of an elastic body under large applied forces. Now, imagine a small local wave-like perturbation (dotted curve in Figure 3) superimposed on the deformed pattern at the measured point. The ensuing

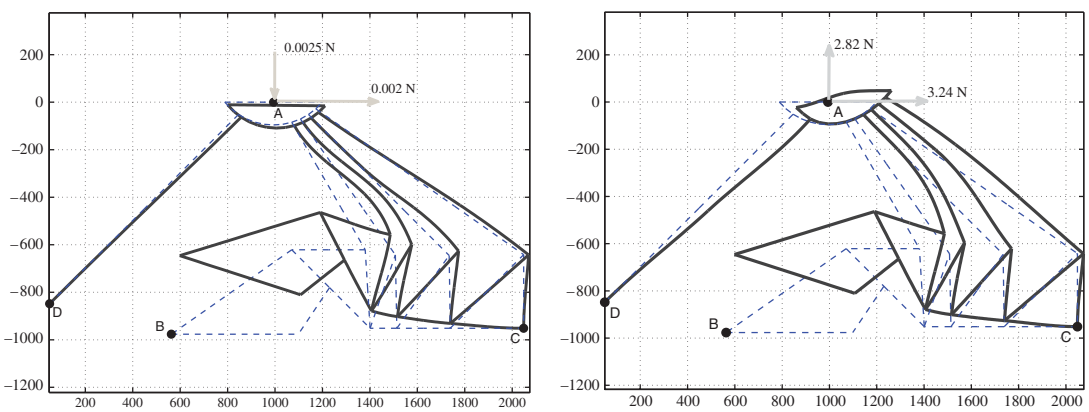

Figure 2. An example to show the non-uniqueness of loading for a given displacement at a point B when the locations of the applied forces are known. The geometry and material data of this displacement-amplification compliant mechanism are given in Appendix A.2.

DOI: 10.1002/nme

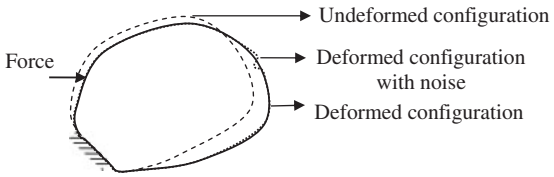

Figure 3. An example to illustrate the lack of continuity in the computed forces for small changes in the measured displacements. The same force is unlikely to give the dotted curve even if the waviness is very small as compared with the gross deformation; many local forces of large magnitudes and alternating directions are required to give the wavy-deformed profile.

large changes in the local curvature at the measured point would require a significantly different force distribution. This force distribution should also be wavy with large amplitudes in opposing directions to effect the small local wave-like change in the deformed profile. This is pictorially illustrated in Figure 3.

1.1. Related work

Oda and Moto [12] presented the problem of determining contact stress distributions based on measured strains or displacements far away from the contact region. In the last two decades, one of the first papers to appear on the reconstruction-type inverse elasticity problem was by Maniatty *et al.* [13]. The method used in that study was to minimize the least squares error between measured and computed displacements along with imposing smoothness on the computed forces on the boundary. They used the finite element framework. Later, Zabaras *et al.* [14] used boundary element method (BEM) and introduced a systematic way to construct regularization matrices for smoothening the computed forces on the boundary. They called it spatial smoothening. Schnur and Zabaras [7] assumed a polynomial distribution for the computed forces and compared the results with those of spatial regularization. They noted that knowing the regularization parameter *a priori* is difficult. In [15], it was shown that the spatial regularization method is equivalent to the Bayesian statistical model if the input data have Gaussian distribution and the error in it is uncorrelated. Bezerra and Saigal [16] solved the problem in the framework of BEM and considered cases wherein the location of the applied force is not assumed. Martin *et al.* [17] took advantage of the linearity of the problem and used singular value decomposition (SVD) to solve the problem in a single step using BEM. Zhang *et al.* [18] used BEM to reconstruct the boundary force for known strains at few locations in the interior of the domain for the 3D case. Lu and Rizzo [19] used the framework of BEM to solve the problem for the unknown boundary force using SVD, as was done in [17] except that they also measured strains along with the displacements. Turco [20] developed a method to reconstruct boundary forces using B-spline BEM-based stress measurement at a few locations. Nakagiri and Suzuki [21] discussed the effect of errors in measured displacements on the computed forces using sensitivity analysis. Recently, Turco [22] compared statistical and deterministic approaches to this problem and arrived at similar conclusions as those in [15]. In addition to finite element method and BEM, meshless methods have also been used to solve this problem [23].

The iterative methods for solving the Cauchy problem for elliptic equations have been extensively investigated for Laplace equation as well as for elasticity equation [24]. In particular, Kozlov *et al.* [24] proposed an iterative method for the Cauchy problem in elasticity in which two problems are alternately solved until consistent solution between known displacements and forces is found.

DOI: 10.1002/nme

One problem assumes the known displacements and computes the force while the other problem assumes the known forces and computes the displacements. In recent years, this method was used by Marine [23] and Baranger and Andrieux [25]. Belgacem and co-researchers [26, 27] recently proposed a variational approach to solving the Cauchy problem for Laplace operator in the framework of Steklov–Poincaré theory. A passing remark made in [26] about pre-conditioning the known Dirichlet data has some resemblance to the approach taken by us.

There is also a body of literature in vision-based force-sensing that does not follow the solution approach of the aforementioned papers. In [1], the displacements at all points of an elastic body undergoing large deformation were used to determine the applied forces and their locations. Their sensitivity analysis found that the logarithmic strain measure that was used turned out to be highly sensitive to errors in the measured displacement data. Greminger and Nelson [2] solved this problem by using a deformable template matching technique. Kamiyama *et al.* [3] estimated the unknown forces acting on a plate by using superposition of Boussinesq solution at multiple points.

1.2. Scope of this study

All the aforementioned papers (except [1]) considered geometrically linear (i.e. small displacements) elastic problem. In this paper, we consider geometrically non-linear elastic deformations. This is because, as noted above, we solve Cauchy's elasticity problem and use it as a vision-based force-sensing technique. Noting that the errors in displacement measurement are inevitable, the relative error can be decreased by making the elastic structure sufficiently flexible. Thus, we use compliant mechanisms [28] that are custom-designed for undergoing large deformations within the yield stress limit.

We present two methods in this paper. The first method (called the direct pseudo-inverse method) is similar to the method presented in [19] and one-step method presented in [17]. However, our method necessarily becomes iterative because of the consideration of the geometric non-linearity. Numerical examples and experiments that we conducted indicate that this method, similar to the earlier methods, is prone to errors when deformations are large and when there is large noise in the data even in the case of small deformation. Therefore, the second method takes a new approach to solve the Cauchy problem: here, we pose an optimization problem wherein small perturbations in the measured displacements become the variables that are adjusted to minimize the spurious forces at the measured locations. This is equivalent to pre-conditioning the measured noisy displacements as was alluded to in [26] with symmetry arguments. This method helps in smoothening the displacements making the method less vulnerable to the noise in the measured displacement data. Both the methods assume the locations of the forces and a function form for the boundary forces and use the finite element framework.

The remainder of the paper is organized as follows. In Section 2, a clear statement of the problem and the assumptions are noted. The first method using the direct pseudo-inverse method is presented in Section 3. The second method that minimizes the spurious forces by adjusting the measured displacements is described in Section 4. Results and discussion are in Section 5 followed by concluding remarks in Section 6.

2. STATEMENT OF THE PROBLEM

Domain Ω of the elastic body under consideration is partitioned into two regions, one where displacements are measured (Ω_{measured}) and the other, denoted by Ω_{free}, is the complement of

DOI: 10.1002/nme

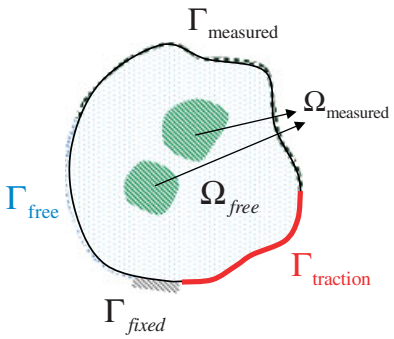

Figure 4. Partitioning of the domain and its boundary for the elastic body based on measured displacement data and known locations of the force.

Ω_{measured}. Additionally, the boundary Γ is partitioned into four parts, the first where the forces act (Γ_{traction}), the second where the displacements are measured (Γ_{measured}), the third where the boundary is fixed (Γ_{fixed}), and the fourth is the complement of the union of the first three and is denoted by Γ_{free}. It should be noted that $\Gamma_{\text{measured}} \cup \Gamma_{\text{free}}$ is free from applied forces. All these partitions of the domain and its boundary are shown in Figure 4. The mathematical statement of the problem considered in this paper can be stated as follows:

$$\nabla \cdot \tilde{\mathbf{T}} = 0 \quad \text{in } \Omega \tag{1a}$$

$$\tilde{\mathbf{T}} = \lambda \operatorname{tr}(\tilde{\mathbf{E}})\tilde{\mathbf{I}} + 2\mu\tilde{\mathbf{E}} \tag{1b}$$

$$\tilde{\mathbf{E}} = \tfrac{1}{2}(\nabla\mathbf{U} + \nabla\mathbf{U}^{\mathrm{T}} + \nabla\mathbf{U}^{\mathrm{T}}\nabla\mathbf{U}) \tag{1c}$$

$$\mathbf{U} = 0 \quad \text{on } \Gamma_{\text{fixed}} \tag{1d}$$

$$\mathbf{t} = 0 \quad \text{on } \Gamma_{\text{measured}} \cup \Gamma_{\text{free}} \tag{1e}$$

$$\mathbf{U} = \mathbf{U}_{\text{measured}} \quad \text{on } \Omega_{\text{measured}} \cup \Gamma_{\text{measured}} \tag{1f}$$

where $\tilde{\mathbf{T}}$ is the second Piola–Kirchoff stress tensor, $\tilde{\mathbf{I}}$ the identity tensor, $\tilde{\mathbf{E}}$ the Green strain tensor, λ and μ the Láme constants of the material, $\mathbf{U}$ the displacement vector, $\mathbf{t}$ the traction, and $\mathbf{U}_{\text{measured}}$ the measured displacement vector. Although the problem stated in Equations (1a)–(1f) may appear to be the standard elasticity problem, as mentioned earlier, it is significantly different because of Equations (1e)–(1f). It should be noted that, on Γ_{measured}, we not only know the displacements from the measurement but also know the forces to be zero. On the other hand, on Γ_{traction}, we know neither displacements nor forces. Because of these two deviations from the usual elasticity problem, the solution procedure for solving Equations (1a)–(1f) needs to be different. Before we present the two methods of solution in Sections 3 and 4, we define the notation used in the discretized finite element model.

Figure 5 schematically shows the discretized finite element model of the elastic body considered in this study. We denote the set of finite-element degrees of freedom (dof) that belong to Γ_{traction} as R_1, the dof that belong to $\Omega_{\text{measured}} \cup \Gamma_{\text{measured}}$ as R_2, and the remaining dof belonging to $\Omega_{\text{free}} \cup \Gamma_{\text{free}}$ as R_3. The dof corresponding to Γ_{fixed} are not included here because they will be eliminated in obtaining the reduced tangent stiffness matrix (see Appendix A.1). By denoting the

DOI: 10.1002/nme

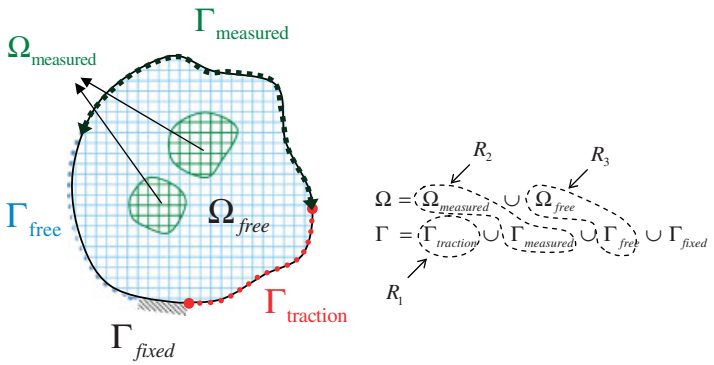

Figure 5. Schematic of the discretized finite element model of the elastic body. The partition of the dof in the discretized model is also shown. Γ_{fixed} is not grouped because it is taken care of by working with the reduced stiffness matrix wherein specified displacements (Dirichlet boundary conditions) are already imposed.

internal forces corresponding to the aforementioned three sets of dof as $\mathbf{F}_{\text{int}}$, the displacements by $\mathbf{u}$, and their corresponding incremented quantities with a suffix Δ, the discretized static equilibrium equations can be expressed as follows:

$$\mathbf{F}_{\text{int}} = \mathbf{F}_{\text{ext}} \tag{2}$$

As per the above notation, $\mathbf{F}_{\text{int}}$ and $\mathbf{F}_{\text{ext}}$ are split into three components corresponding to the three aforementioned sets:

$$\mathbf{F}_{\text{int}} = \begin{Bmatrix} \mathbf{F}_1 \\ \mathbf{F}_2 \\ \mathbf{F}_3 \end{Bmatrix}_{\text{int}}, \quad \mathbf{F}_{\text{ext}} = \begin{Bmatrix} \mathbf{F}_1 \\ \mathbf{F}_2 \\ \mathbf{F}_3 \end{Bmatrix}_{\text{ext}} = \begin{Bmatrix} \mathbf{F}_1 \\ \mathbf{0} \\ \mathbf{0} \end{Bmatrix}_{\text{ext}} \tag{3}$$

We also note that only $\mathbf{F}_{1\text{ext}}$ is non-zero because we know that there are no external forces on the other two sets of dof. By considering the first-order Taylor series for $\mathbf{F}_{\text{int}}$, we obtain

$$\mathbf{F}_{\text{int}} + \frac{\partial \mathbf{F}_{\text{int}}}{\partial \mathbf{u}} \Delta \mathbf{u} = \mathbf{F}_{\text{int}} + \mathbf{K}_t \Delta \mathbf{u} = \mathbf{F}_{\text{ext}} \tag{4}$$

where $\mathbf{K}_t$ is the tangent stiffness matrix, which depends on $\mathbf{u}$ in geometrically non-linear problems. The details of how we compute $\mathbf{F}_{\text{int}}$ and $\mathbf{K}_t$ are provided in Appendix A.1. The linearization of the internal force, as shown in Equation (4), helps us solve Equation (2) iteratively. In each iteration, the change in the computed displacements, $\Delta\mathbf{u}$, is obtained by solving the following equation:

$$\mathbf{K}_t \Delta \mathbf{u} = \mathbf{F}_{\text{ext}} - \mathbf{F}_{\text{int}} \;\Rightarrow\; \begin{bmatrix} \mathbf{K}_{11} & \mathbf{K}_{12} & \mathbf{K}_{13} \\ \mathbf{K}_{21} & \mathbf{K}_{22} & \mathbf{K}_{23} \\ \mathbf{K}_{31} & \mathbf{K}_{32} & \mathbf{K}_{33} \end{bmatrix} \begin{Bmatrix} \Delta \mathbf{u}_1 \\ \Delta \mathbf{u}_2 \\ \Delta \mathbf{u}_3 \end{Bmatrix} = \begin{Bmatrix} \mathbf{F}_1 \\ \mathbf{0} \\ \mathbf{0} \end{Bmatrix}_{\text{ext}} - \begin{Bmatrix} \mathbf{F}_1 \\ \mathbf{F}_2 \\ \mathbf{F}_3 \end{Bmatrix}_{\text{int}} = \begin{Bmatrix} \Delta \mathbf{F}_{1\text{c}} \\ \Delta \mathbf{F}_{2\text{c}} \\ \Delta \mathbf{F}_{3\text{c}} \end{Bmatrix} \tag{5}$$

where $\Delta\mathbf{F}_{\text{c}}$ is the change in the forces to correct the displacements iteratively to satisfy Equation (2) at convergence. Equation (5) also shows the tangent stiffness matrix broken down into its

DOI: 10.1002/nme

constituents corresponding to the three sets. Now, the problem reduces to determining $\mathbf{F}_{1\text{ext}}$. Equation (5) will be used in the two methods of solution to this problem as presented in the following two sections.

3. DIRECT PSEUDO-INVERSE METHOD (DPIM)

The main idea of this method is to keep the measured displacement vector, $\mathbf{u}_2$, unchanged even though we know that there might be measurement errors in it. Therefore, in the iterative procedure to solve the problem in Equation (2), when we use the linearized iterative equation (i.e. Equation (5)), $\Delta\mathbf{u}_2$ will be a null vector:

$$\begin{bmatrix} \mathbf{K}_{11} & \mathbf{K}_{12} & \mathbf{K}_{13} \\ \mathbf{K}_{21} & \mathbf{K}_{22} & \mathbf{K}_{23} \\ \mathbf{K}_{31} & \mathbf{K}_{32} & \mathbf{K}_{33} \end{bmatrix} \begin{Bmatrix} \Delta\mathbf{u}_1 \\ \mathbf{0} \\ \Delta\mathbf{u}_3 \end{Bmatrix} = \begin{Bmatrix} \mathbf{F}_1 \\ \mathbf{0} \\ \mathbf{0} \end{Bmatrix}_{\text{ext}} - \begin{Bmatrix} \mathbf{F}_1 \\ \mathbf{F}_2 \\ \mathbf{F}_3 \end{Bmatrix}_{\text{int}} = \begin{Bmatrix} \Delta\mathbf{F}_{1\text{c}} \\ \Delta\mathbf{F}_{2\text{c}} \\ \Delta\mathbf{F}_{3\text{c}} \end{Bmatrix} \tag{6}$$

We initiate the method by assuming that $\mathbf{u}_1$ and $\mathbf{u}_3$ are null vectors and $\mathbf{u}_2$ is the measured displacement vector. Using these, we compute $\mathbf{F}_{\text{int}}$. Now, by using the last row of Equation (6), we obtain

$$\Delta\mathbf{u}_3 = \mathbf{K}_{33}^{-1}(\Delta\mathbf{F}_{3\text{c}} - \mathbf{K}_{31}\Delta\mathbf{u}_1) = \mathbf{K}_{33}^{-1}(-\mathbf{F}_{3\text{int}} - \mathbf{K}_{31}\Delta\mathbf{u}_1) \tag{7}$$

By substituting $\Delta\mathbf{u}_3$ from Equation (7) into the second row of Equation (6), we obtain

$$\begin{aligned} [\mathbf{K}_{21} - \mathbf{K}_{23}\mathbf{K}_{33}^{-1}\mathbf{K}_{31}]\{\Delta\mathbf{u}_1\} &= \{\Delta\mathbf{F}_{2\text{c}} - \mathbf{K}_{23}\mathbf{K}_{33}^{-1}\Delta\mathbf{F}_{3\text{c}}\} \\ &= \{-\mathbf{F}_{2\text{int}} + \mathbf{K}_{23}\mathbf{K}_{33}^{-1}\mathbf{F}_{3\text{int}}\} \end{aligned} \tag{8}$$

Because $[\mathbf{K}_{21} - \mathbf{K}_{23}\mathbf{K}_{33}^{-1}\mathbf{K}_{31}]$ is not a square matrix in general, we need to use pseudo-inverse to solve Equation (8). After this, we substitute $\Delta\mathbf{u}_1$ and $\Delta\mathbf{u}_3$ from Equations (8) and (7), respectively, into the first row of Equation (6) to compute $\Delta\mathbf{F}_{1\text{c}}$. This correction is used to compute the unknown external force on the traction boundary:

$$\mathbf{F}_{1\text{ext}} = \Delta\mathbf{F}_{1\text{c}} + \mathbf{F}_{1\text{int}} \tag{9}$$

Now, we also update the displacements, $\mathbf{u}_1$ and $\mathbf{u}_3$:

$$\begin{aligned} \mathbf{u}_1^{\text{new}} &= \Delta\mathbf{u}_1 + \mathbf{u}_1^{\text{old}} \\ \mathbf{u}_3^{\text{new}} &= \Delta\mathbf{u}_3 + \mathbf{u}_3^{\text{old}} \end{aligned} \tag{10}$$

Note that $\mathbf{u}_2$ does not need to be updated because in this method we assume that $\Delta\mathbf{u}_2$ is a null vector as noted above. This procedure is repeated until the norms of $\Delta\mathbf{u}_1$ and $\Delta\mathbf{u}_3$ are negligibly small.

When the above algorithm converges, $\mathbf{F}_{3\text{int}}$ is driven to a null vector because the third row of Equation (6) is exactly satisfied. However, $\mathbf{F}_{2\text{int}}$ in general does not approach a null vector because of the pseudo-inverse solution of the second row of Equation (6). This issue is addressed in our second method. This issue aside, it should be noted that there is no guarantee that this iterative algorithm always converges. Hence, we modify this below by assuming a function form for $\mathbf{F}_{1\text{ext}}$.

DOI: 10.1002/nme

Assuming a suitable function form of an unknown quantity in inverse problems leads to regularization. For example, Schnur and Zabaras [7] and Bezerra and Saigal [16] assumed the function form for the unknown force and obtained regularized solution. The way in which we use the function form for the unknown forces is different from these two and other papers because the solution procedure presented above is different.

For a chosen function form on Γ_{traction}, in the discretized finite element model, we can express the following:

$$\{\mathbf{F}_{1\text{ext}}\} = [\mathbf{P}]\{\mathbf{a}\} \tag{11}$$

where $\mathbf{P}$ is a coefficient matrix that fits the function form onto the discretized model and $\mathbf{a}$ is the vector of unknown coefficients in the assumed function form. Now, since $\mathbf{F}_{1\text{ext}} = \mathbf{F}_{1\text{int}}$, we define a least squares error, ε, for $\mathbf{F}_{1\text{int}}$:

$$\varepsilon = (\mathbf{Pa} - \mathbf{F}_{1\text{int}})^{\mathrm{T}}(\mathbf{Pa} - \mathbf{F}_{1\text{int}}) \tag{12}$$

Minimization of this error with respect to $\mathbf{a}$ yields

$$\frac{\partial \varepsilon}{\partial \mathbf{a}} = \mathbf{0} \;\Rightarrow\; \mathbf{a} = [\mathbf{P}^{\mathrm{T}}\mathbf{P}]^{-1}\mathbf{P}^{\mathrm{T}}\mathbf{F}_{1\text{int}} \tag{13}$$

By substituting the value of $\mathbf{a}$ from Equation (13) into Equations (11) and (9), we obtain an estimate for $\Delta\mathbf{F}_{1\text{c}}$ as follows:

$$\Delta\mathbf{F}_{1\text{c}} = \mathbf{Pa} - \mathbf{F}_{1\text{int}} = [\mathbf{P}(\mathbf{P}^{\mathrm{T}}\mathbf{P})^{-1}\mathbf{P}^{\mathrm{T}} - \mathbf{I}]\mathbf{F}_{1\text{int}} \tag{14}$$

This is an additional piece of information in solving Equation (6). Previously, only the second row was used to compute $\Delta\mathbf{u}_1$ as shown in Equation (8). Now, we use the additional information in Equation (14) (which came from the assumed function form of $\mathbf{F}_{1\text{ext}}$) by using the first and second rows of Equation (6) simultaneously to compute $\Delta\mathbf{u}_1$:

$$\begin{bmatrix} \mathbf{K}_{11} - \mathbf{K}_{13}\mathbf{K}_{33}^{-1}\mathbf{K}_{31} \\ \mathbf{K}_{21} - \mathbf{K}_{23}\mathbf{K}_{33}^{-1}\mathbf{K}_{31} \end{bmatrix} \{\Delta\mathbf{u}_1\} = \begin{Bmatrix} [\mathbf{P}(\mathbf{P}^{\mathrm{T}}\mathbf{P})^{-1}\mathbf{P}^{\mathrm{T}} - \mathbf{I}]\mathbf{F}_{1\text{int}} + \mathbf{K}_{13}\mathbf{K}_{33}^{-1}\mathbf{F}_{3\text{int}} \\ -\mathbf{F}_{2\text{int}} + \mathbf{K}_{23}\mathbf{K}_{33}^{-1}\mathbf{F}_{3\text{int}} \end{Bmatrix} \tag{15}$$

This modification is an improvement over the earlier procedure because it ensures that the computed traction follows the known function form. However, there is an inherent problem in this method, which is also applicable to other methods. The problem is that unwanted forces arise at the displacement measurement points. This is because even the modified algorithm (i.e. Equation (15)) does not make $\mathbf{F}_{2\text{int}}$ a null vector, especially when the errors in the measured displacements are large. The non-zero value of $\mathbf{F}_{2\text{ext}}$, which is equal to $\mathbf{F}_{2\text{int}}$ when $\Delta\mathbf{F}_{2\text{c}}$ becomes zero at convergence, leads to spurious forces on the measured dof (i.e. R_2 in Figure 5). These forces are called spurious because we assumed that there are no external forces at the measured dof. The first numerical example in Section 5 illustrates the effect of noise on the appearance of spurious forces. In the following section, we present a method that minimizes such spurious forces.

4. METHOD OF MINIMIZING SPURIOUS FORCES (MMSF)

In Section 1, we note that a small perturbation in the measured displacement data necessitates a large change in the computed force to accommodate that perturbation. This is also pictorially

DOI: 10.1002/nme

illustrated in Figure 3. Earlier work focused on regularizing the computed force. Here, we want to regularize/pre-condition the measured displacement itself because we know that measured displacement data using computer vision would inevitably be noisy. We do this by allowing small perturbations in the measured displacement data, $\mathbf{u}_2$. We use these perturbations as variables in an optimization problem that minimizes the norm of the spurious forces that arise at the measured dof, $\mathbf{F}_2$. Thus, this method is called the method of minimizing spurious forces (MMSF). It helps pre-condition the measured displacement data while helping also to regularize the computed force data. The minimization problem is mathematically stated as follows:

$$\begin{aligned} &\underset{\mathbf{u}_{2a}}{\text{Minimize}} \quad \mathbf{F}_2^{\mathrm{T}}\mathbf{F}_2 \\ &\text{Subject to} \quad \mathbf{u}_{2a}^{\min} \leqslant \mathbf{u}_{2a} \leqslant \mathbf{u}_{2a}^{\max} \end{aligned} \tag{P1}$$

where

$$\begin{aligned} \mathbf{u}_{2a}^{\min} &= (1-\eta/100)\mathbf{u}_2 \\ \mathbf{u}_{2a}^{\max} &= (1+\eta/100)\mathbf{u}_2 \end{aligned} \tag{16}$$

with η denoting the maximum percent error in the measured data.

The method of computing $\mathbf{F}_2$ in problem (P1) is the same as the DPIM presented in Section 3 with the difference that $\mathbf{u}_2 = \mathbf{u}_{2a}$. This means that in each iteration of the optimization procedure, we need to solve DPIM once. In order to make the optimization solution procedure computationally efficient, we compute the gradients of the objective function analytically (instead of using finite difference methods) as shown below.

4.1. Analytical computation of the gradients

The gradient of the objective function in problem (P1) is given by

$$\frac{\partial(\mathbf{F}_2^{\mathrm{T}}\mathbf{F}_2)}{\partial \mathbf{u}_2} = 2\frac{\partial(\mathbf{F}_2^{\mathrm{T}})}{\partial \mathbf{u}_2}\mathbf{F}_2 \tag{17}$$

By using the second and third rows of Equation (5), we obtain

$$\Delta\mathbf{F}_{2c} = [\mathbf{K}_{22} - \mathbf{K}_{23}\mathbf{K}_{33}^{-1}\mathbf{K}_{32}]\Delta\mathbf{u}_2 + [\mathbf{K}_{21} - \mathbf{K}_{23}\mathbf{K}_{33}^{-1}\mathbf{K}_{31}]\Delta\mathbf{u}_1 + \mathbf{K}_{23}\mathbf{K}_{33}^{-1}\Delta\mathbf{F}_{3c} \tag{18}$$

From Equations (18) and (17), the gradient can now be obtained as

$$\frac{\partial(\mathbf{F}_2^{\mathrm{T}}\mathbf{F}_2)}{\partial \mathbf{u}_2} = 2[\mathbf{K}_{22} - \mathbf{K}_{23}\mathbf{K}_{33}^{-1}\mathbf{K}_{32}]\mathbf{F}_2 \tag{19}$$

The `fmincon` routine in the MATLAB optimization toolbox was used to solve the optimization problem. Sequential quadratic programming combined with the trust region method is used by `fmincon`. Results of DPIM and MMSF are presented in the following section.

5. RESULTS AND DISCUSSION

In this section, seven numerical examples and one experimental example are presented. In the numerical examples, the displacement data are generated numerically by using the computed

DOI: 10.1002/nme

displacements with known applied forces. Thus, in these examples we know the correct values of the forces. Then, 'noise' is added to it using `rand` function in Matlab. The noise level is varied by using $\eta\%$ to study the effects of increased noise. The `rand` function gives a value within the range [0, 1]. Therefore, $\mathbf{u}_2$ with noise can be expressed as follows:

$$\mathbf{u}_{2_i}^{\text{noisy}} = \left(1 + \frac{(-1+2(\text{rand}))\eta}{100}\right)\mathbf{u}_{2_i} \tag{20}$$

where the subscript i refers to the ith dof. Thus, the `rand` function is invoked separately for each dof in $\mathbf{u}_2$. This gives non-uniform noise over the measured portion of the elastic body, which is more realistic than giving the same noise everywhere. The noisy data generated in this manner are used to estimate the forces. This helps in validating the accuracy of the two methods presented in this paper. We used 4-noded and 9-noded quadrilateral elements as well as co-rotational 2D beam elements. The elastic bodies considered are an arch beam, a rectangular sheet, a displacement-amplification compliant mechanism, and a slender rectangular sheet that acts like a cantilever. All the numerical examples were solved using both DPIM and MMSF. The experimental example was solved using only MMSF, which is superior to DPIM.

5.1. Example 1: an effect of the noise and motivation for MMSF

Figures 6 and 7 show the effect of uniform and non-uniform noise in the displacement data on the computed force data. The error in the computed force data is much more when the noise in the displacement data is non-uniform. The inset in Figure 7 illustrates this. We consider an arch beam example to see the impact of the noise on spurious forces and in turn on estimated force. The geometry of the arch beam is shown in Figure 8. It has inner and outer radii of 4 and 5 mm, respectively, and 1 mm out-of-plane thickness. It is assumed to be made of a material with Young's modulus of 200 MPa and Poisson's ratio of 0.33. The beam is discretized into a mesh of 40×3 elements as shown in Figure 8. In these tests we assume that the applied forces are acting at point '**A**,' which is also shown in the figure. We generated seven cases for one random error and this procedure is repeated for several random errors. Displacements are noted at seven locations, which are shown in Figure 8 with black dots labelled 1–7. We have also tested for uniform error. Spurious forces

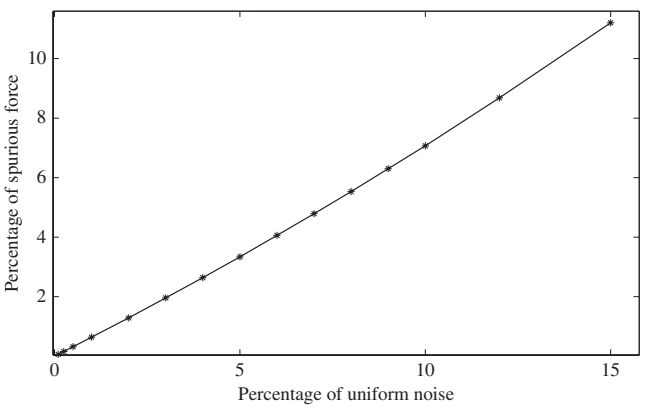

Figure 6. Percentage of spurious forces under uniform noise.

DOI: 10.1002/nme

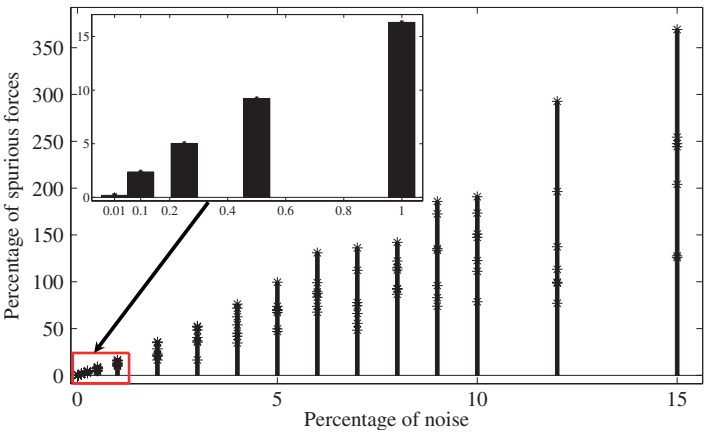

Figure 7. Percentage of spurious forces under random noise.

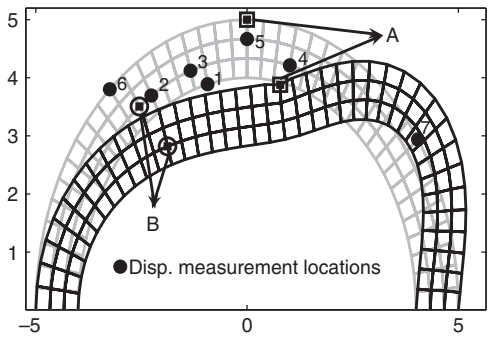

Figure 8. Deformed and undeformed configurations with displacement measurement locations.

corresponding to the cases of random and uniform noise are shown in Figures 6 and 7. In these cases, we observed that local curvature change makes spurious forces high and it affects the estimated force in order to satisfy static equilibrium (i.e. the sum of force has to be zero). Upon minimization of the spurious forces, it takes the shape with minimum curvature changes. In general, we cannot ensure that measured displacements approach towards the exact displacements; rather we can see that it travels towards minimum curvature change within given bounds. The percentage of spurious force is defined as the ratio of the l_2-norm of the spurious forces and the l_2-norm of the applied forces. We introduced percentage of error in the displacements using random number generator. One observation in this numerical experiment is that 3% is the tolerable limit for the spurious forces.

5.2. Example 2: an arch beam problem with continuum 4-node quad element

We consider the same arch beam of Figure 8 here. The numbers of dof corresponding to x and y displacements at point A are 287 and 288, respectively. The beam is held fixed at the two bottom ends making it a fixed-fixed arch beam.

DOI: 10.1002/nme

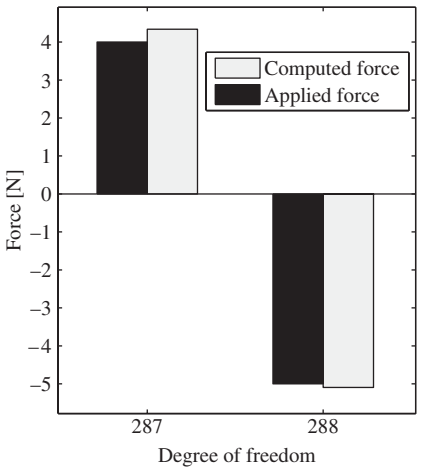

Figure 9. Computed forces for arch beam.

In the first numerical test, we consider that the x and y displacements are noted at location B, which is shown in Figure 8. The value of η was set at 10%. Forces are computed using noisy displacements by DPIM. The error in the computed force is 8.4% in the horizontal direction and 1.9% in the vertical direction. Computed forces are shown in Figure 9.

In the second test, we consider two cases, one with 5% random error and the other with 10% random error. Displacements are noted at seven locations and are shown in Figure 6 with black dots labelled 1–7. The dof of these measured locations are $2i-1$ and $2i$ along x and y directions, respectively, where i is the node number, which is shown in Figure 8 as a label next to the black dot. The forces were estimated using both DPIM and MMSF for $\eta=5$ and 10%. For $\eta=5\%$, DPIM gave 23.08% error in the computed force (see Figure 10(a)) while MMSF had an error of only 1.96% (see Figure 10(b)). For $\eta=10\%$, the errors were 176.29% (see Figure 11(a)) for DPIM and 1.61% for MMSF (see Figure 11(b)). It is worth noting that DPIM reversed even the sign of the force. The reason for the large forces in DPIM for large noise is mainly due to increased spurious forces at the measured points. These are shown in Table I. As can be seen in Table I, MMSF minimizes them and gives good results.

5.3. Example 3: an arch beam problem with a co-rotational beam element

We consider another arch beam with a radius of 20 mm, area (**A**) of 0.6 mm^2, and moment of inertia (**I**) of 0.018 mm^4. Material properties of the beam are taken as 200 MPa for Young's modulus and 0.33 for Poisson's ratio. Co-rotational beam elements are used in this problem. The beam is discretized into 100 elements. Deformed and undeformed configurations are shown in Figure 12 when the load is applied at point P. Displacements are noted at five locations. These locations are indicated in Figure 12. A random noise of 10% is introduced into displacements, which are taken from the forward solution. We have solved the problem using both DPIM and MMSF. It can be observed that the error in the computed force is 6839.87% as can be seen in Figure 13. This large error can be brought down to 2.77% by using MMSF as shown in Figure 14. The spurious forces are shown in Figure 15 and their numerical values are presented in Table II. The claim that we

DOI: 10.1002/nme

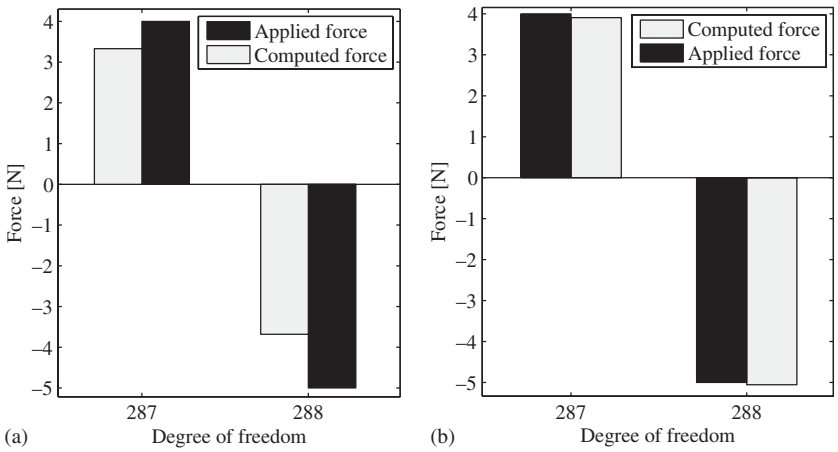

Figure 10. (a) Force response with DPIM with 5% noise and (b) force response with MMSF with 5% noise.

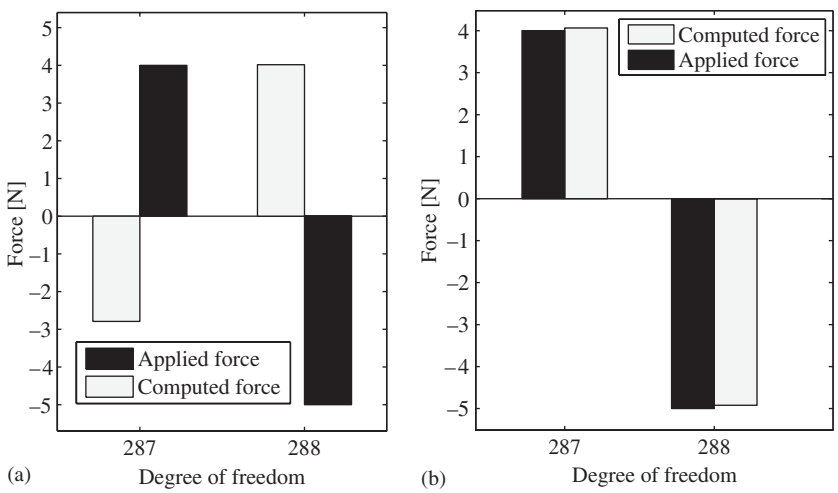

Figure 11. (a) Force response with DPIM with 10% noise and (b) force response with MMSF under 10% noise.

made in the above section is that spurious forces are responsible for deviation in the estimated forces; it is clearly evident from the numerical data presented in the Table II.

5.4. Example 4: a rectangular sheet with a distributed load

We consider a rectangular sheet of 12 and 6 mm along the x direction (horizontal direction) and the y direction (vertical direction), respectively. The domain is discretized with 24×12 quad mesh whose deformed and undeformed configurations are shown in Figure 16. Parts of the bottom boundary of 2 mm of length on both left (i.e. 0–2 mm) and right (i.e. 10–12 mm) sides are fixed,

DOI: 10.1002/nme

Table I. Spurious forces for arch beam with continuum quad elements.

	Forces with DPIM (mN)		Forces with MMSF (mN)	
Node no.	x-Component	y-Component	x-Component	y-Component
1	−0.3405	−24.4766	−0.4004	−0.1135
2	−9.4860	18.1866	−0.1109	0.1109
3	7.9672	−4.0846	−0.2399	0.3462
4	3.9396	3.1629	−0.0646	0.0214
5	2.1004	4.0410	−0.5763	0.5756
6	4.1511	−5.0243	0.0353	−0.5016
7	−0.7566	0.0914	−0.4004	−0.1135

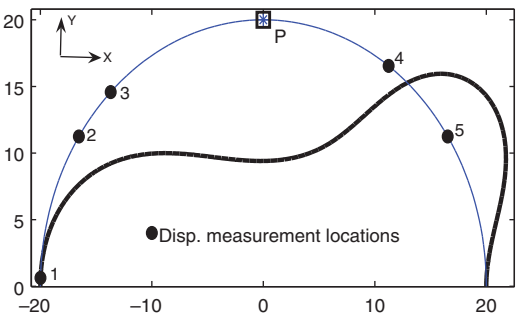

Figure 12. Deformed and undeformed configurations.

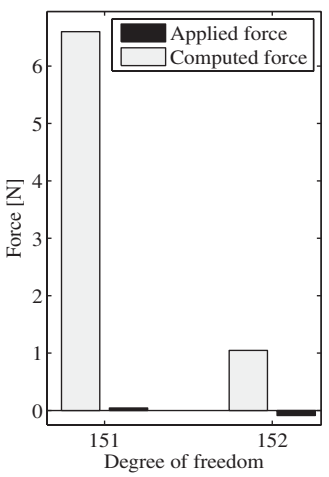

Figure 13. Force response using DPIM with 10% error.

DOI: 10.1002/nme

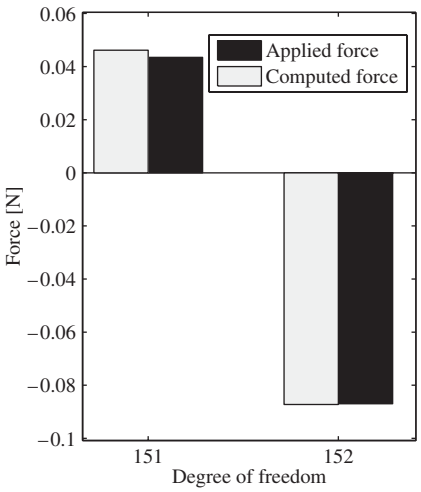

Figure 14. Force response using MMSF with 10% error.

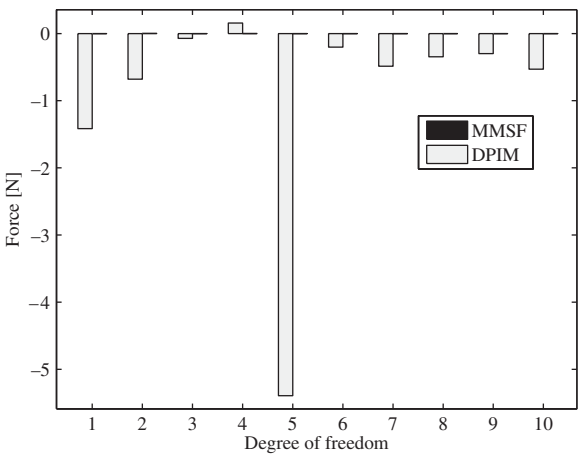

Figure 15. Non-zero force at displacement degree of freedom.

Table II. Spurious forces for arch beam with beam elements.

	Force before MMSF (N)		Force after MMSF ($\times 10^{-3}$) (N)	
Node no.	x-Component	y-Component	x-Component	y-Component
1	−1.4160	−0.6790	−0.2402	2.8296
2	−0.0716	0.1561	−0.1150	1.2074
3	−5.3931	−0.2024	−0.2989	0.0646
4	−0.4870	−0.3454	−0.1343	0.1872
5	−0.2980	−0.5304	−0.2186	0.0403

DOI: 10.1002/nme

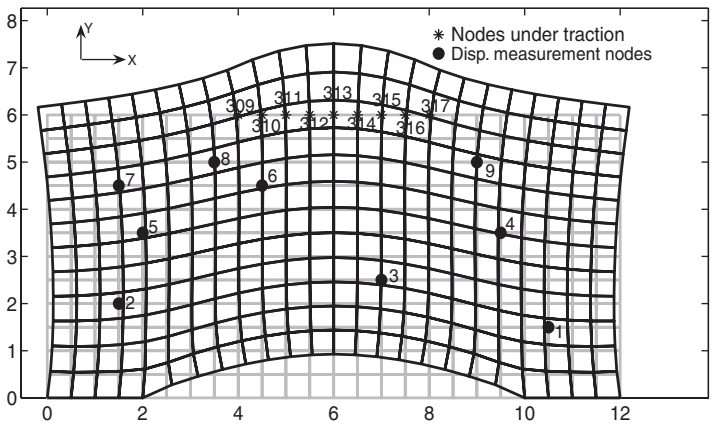

Figure 16. Deformed and undeformed rectangular domain.

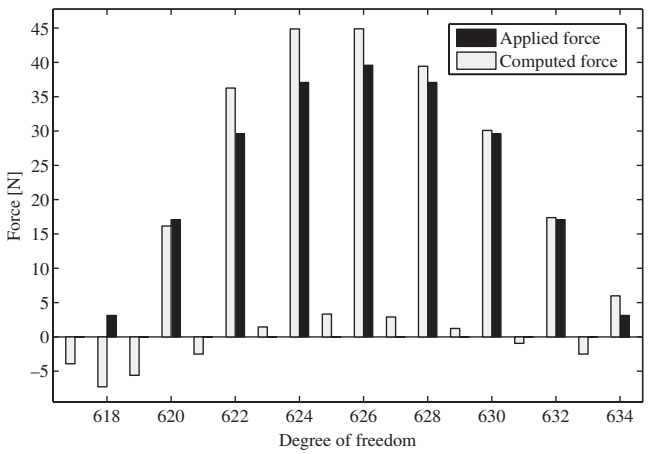

Figure 17. Force response with DPIM under 15% error.

which is evident from deformed configuration. A quadratic distributed load is assumed to be on the top boundary in the middle region of 4 mm length. Nodes under traction are indicated with asterisks on undeformed configuration and are shown in Figure 16. Material constants are taken as 200 MPa for Young's modulus and 0.33 for Poisson's ratio.

We conducted two numerical tests in this problem. In the first test, we noted displacements at nine locations, which are indicated in Figure 16 and these displacement measurements contain 15% random error. We assume that the load distribution is quadratic and it is enforced in the solution procedure. This problem is also solved using DPIM and MMSF. The force response from DPIM is shown in Figure 17 where it can be observed that the error in estimated forces is 22.57%, whereas the error in the forces with MMSF is 5.104%. The force response with MMSF is shown in Figure 18. Once again it is clear that the large error is because of the spurious forces, as can be seen in Figure 19 and Table III. Thus, DPIM gives large errors even for distributed loads.

DOI: 10.1002/nme

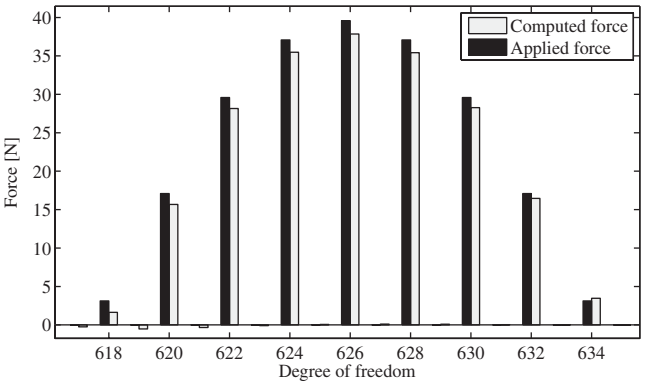

Figure 18. Force response with MMSF under 15% error.

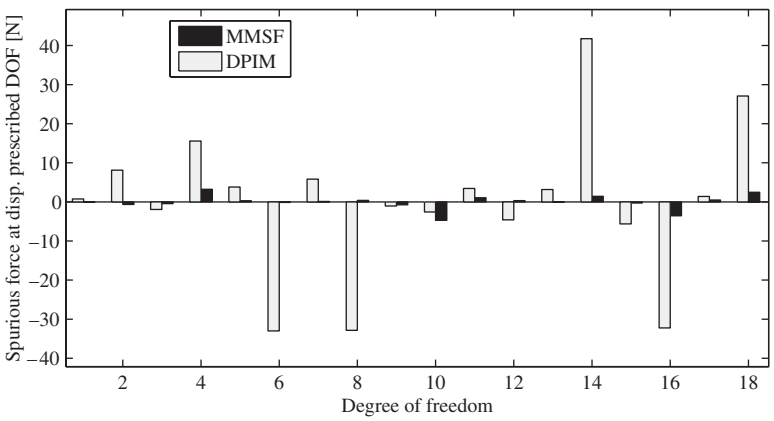

Figure 19. Spurious forces at displacement measurement locations.

Table III. Spurious force for rectangular domain.

	Force before MMSF (N)		Force after MMSF (N)	
Node no.	x-Component	y-Component	x-Component	y-Component
1	7.4152	8.1054	−0.0719	−0.7170
2	−1.9423	15.5759	−0.4560	3.1923
3	3.8049	−33.0147	0.3500	−0.1368
4	5.8221	−32.8605	−0.8026	−4.6725
5	−1.0427	−2.5773	0.0870	0.3707
6	3.4340	−4.6061	1.0799	0.4169
7	3.1715	41.7567	−0.0485	1.4145
8	−5.6324	−32.2386	−0.2833	−3.5546
9	1.4039	27.0852	0.4497	2.4629

DOI: 10.1002/nme

In the second test, we investigated the effect of measurement location on the convergence rate based on the number of iterations. Here, we consider two points A and B, one near the region of application of the load and the other far from the region of application of the load as shown in Figure 20. We computed force using measured displacements at each one of the locations separately without noise.

The distribution of the force is shown in Figure 21. We solved this problem using DPIM because the displacements considered are exact. We observed that 86 iterations are required to converge to the solution if displacement is specified at point B, whereas 19 iterations are sufficient to converge to the solution if displacement is specified at point A. Deformed and undeformed configurations are shown in Figure 16. This indicates that it is better to measure the displacement as close to the load application point as possible.

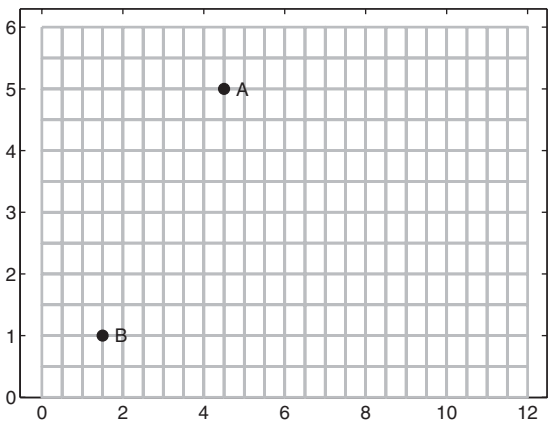

Figure 20. Domain and points A and B.

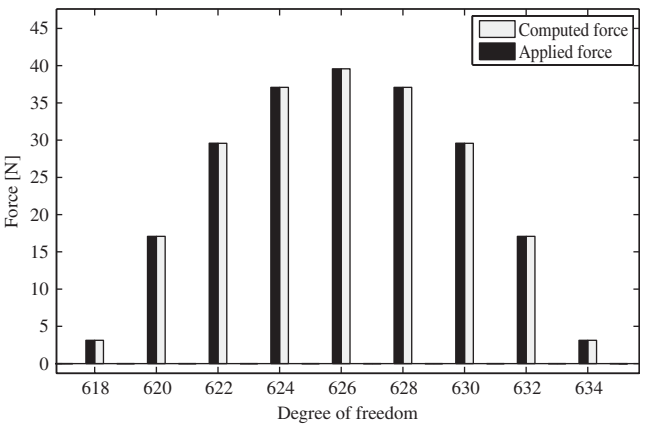

Figure 21. Force distribution.

DOI: 10.1002/nme

5.5. *Example 5: a* Π*-shaped domain with a distributed load*

We consider a Π-shaped domain whose dimensions are shown in Figure 22. The domain is discretized into 608 elements of quad mesh; deformed and undeformed configurations are shown in Figure 23. We have taken the horizontal direction as the x direction and the vertical direction as y direction. The bottom boundary is ($y=0$) of 2 mm length on both the left (i.e. -8 to -6 mm) and the right (i.e. 8–6 mm). A distributed load is assumed to be on the top boundary. Nodes under traction are indicated with squares on undeformed configuration and are shown in Figure 22. Material constants are taken as 200 MPa for Young's modulus and 0.33 for Poisson's ratio.

We noted displacements at 12 locations, which are indicated in Figure 22, and these displacement measurements contain 15% random error. We assume that the load distribution is quadratic in three intervals ($[-12,-7],[-7,7],[7,12]$) and it is enforced in the solution procedure. This problem is also solved using DPIM and MMSF. The force response from DPIM is shown in Figures 24 and 25, where it can be observed that the error in estimated forces is 57.86%, whereas the error in the forces with MMSF is 1.71%. The force response with MMSF is shown in Figures 26 and 27. Once again it is clear that the large error is because of the spurious forces, as shown in Figure 28 and Table IV. Thus, DPIM gives large errors even for distributed loads with assumed function forms.

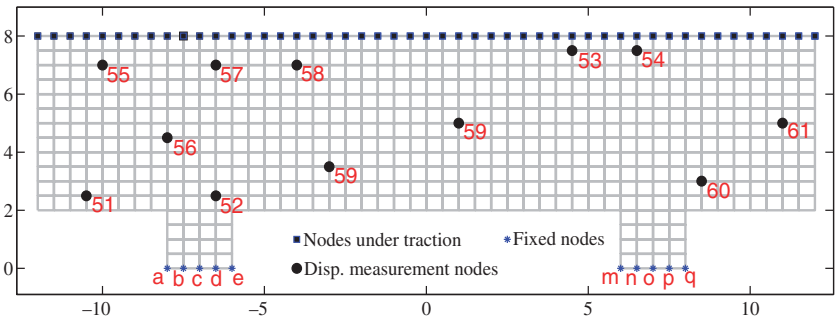

Figure 22. Undeformed Π-domain with boundary conditions.

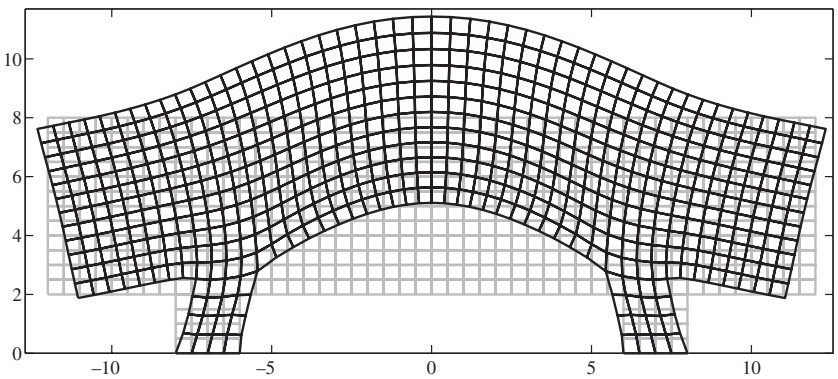

Figure 23. Deformed and undeformed Π-domain.

DOI: 10.1002/nme

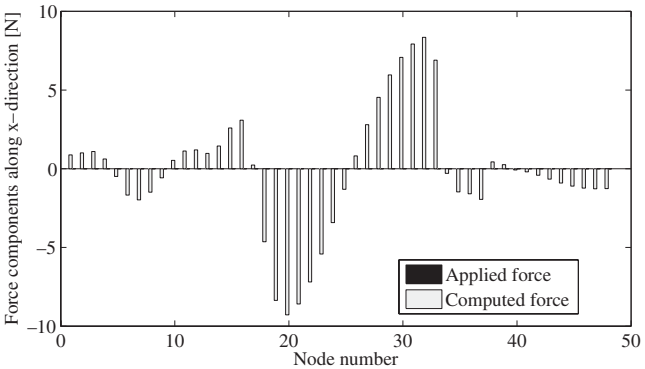

Figure 24. Force response of x-components with DPIM under 15% error.

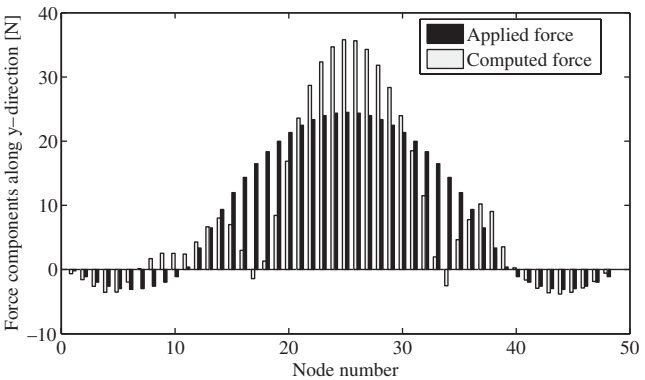

Figure 25. Force response of y-components with DPIM under 15%.

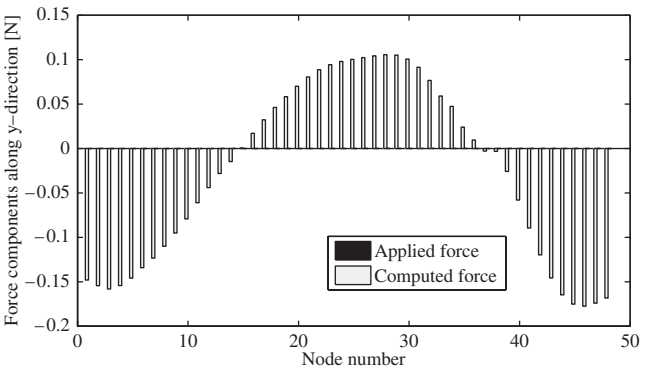

Figure 26. Force response of x-components with MMSF under 15%.

DOI: 10.1002/nme

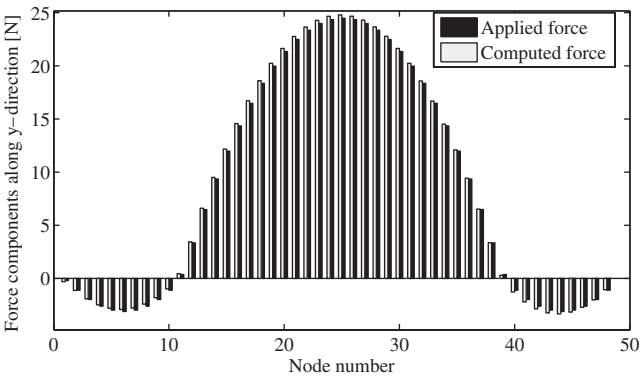

Figure 27. Force response of y-components with MMSF under 15%.

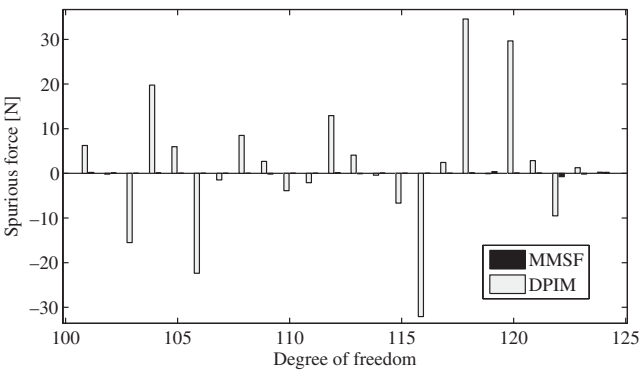

Figure 28. Spurious forces at displacement measurement locations.

Table IV. Spurious force for Π-domain.

	Force before MMSF (N)		Force after MMSF (N)	
Node no.	x-Component	y-Component	x-Component	y-Component
51	6.2307	−0.1657	0.2146	0.0797
52	−15.512	19.7618	0.2146	0.0797
53	5.9692	−22.3640	−0.0246	0.0653
54	−1.4689	8.4871	0.0148	−0.0135
55	2.6791	−3.8736	−0.0226	−0.0189
56	−2.0839	12.9261	−0.1548	0.0005
57	4.0682	−0.4187	0.0065	0.1330
58	−6.6632	−32.0637	−0.0858	0.0349
59	2.4485	34.5737	0.0080	0.0136
60	−0.0774	29.6547	−0.0008	0.0665
61	2.8483	−9.5246	0.3924	0.0405
62	1.2617	0.2423	0.0326	−0.7474

DOI: 10.1002/nme

5.6. Example 6: a displacement amplification compliant mechanism with co-rotational beam elements

We consider the mechanism [11] shown in Figure 29. This problem is carried out with co-rotational beam elements. The out-of-plane thickness of all the beams is 25 μm. The width and the lengths of the beams are given in Appendix A.2. The Young modulus of the material is 200 GPa as opposed to 200 MPa considered so far. The load is applied at point A as shown in the figure. The displacement measurement locations are shown in Figure 29 with black dots. A 10% random noise was added to the data and was solved using DPIM and MMSF. Estimated forces have a very high error of 8370.79% with DPIM as shown in Figure 30. The error in estimated forces comes down to 5.77%

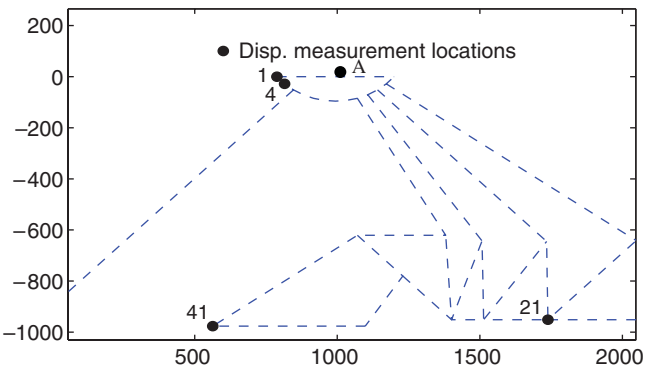

Figure 29. Compliant mechanism with displacement measurement locations.

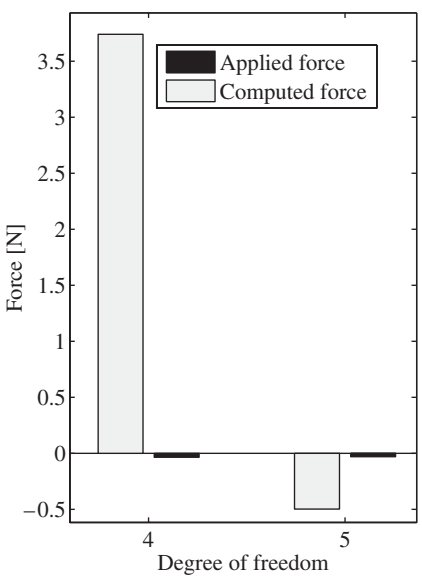

Figure 30. Force response with DPIM under 10% error.

DOI: 10.1002/nme

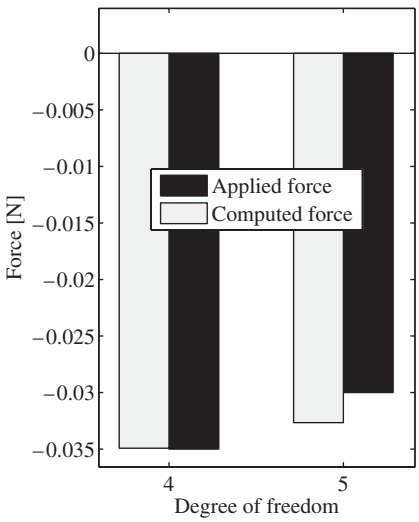

Figure 31. Force response with MMSF under 10% error.

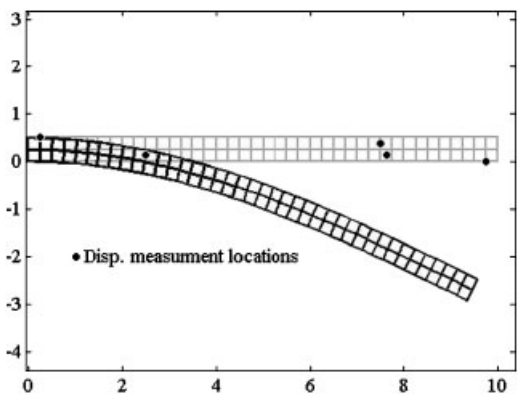

Figure 32. Cantilever beam with displacement measurement locations.

with MMSF as shown in Figure 31. Recall that in Figure 2, the same mechanism was used to illustrate the non-uniqueness of the solution of the inverse problem when only one point is used for displacement measurement. On the basis of this example, we can say that by increasing the number of measurements we can avoid multiple solutions.

5.7. Example 7: a cantilever beam with 9-noded quad elements

Here, we considered a 10 mm long cantilever beam of rectangular cross section of $0.5\,\text{mm} \times 1\,\text{mm}$. A Young modulus of 20 GPa and a Poisson ratio of 0.33 were considered. The beam is discretized into a mesh of 40×2 quad elements as shown in Figure 32. The displacement measurement locations are marked with big dots.

DOI: 10.1002/nme

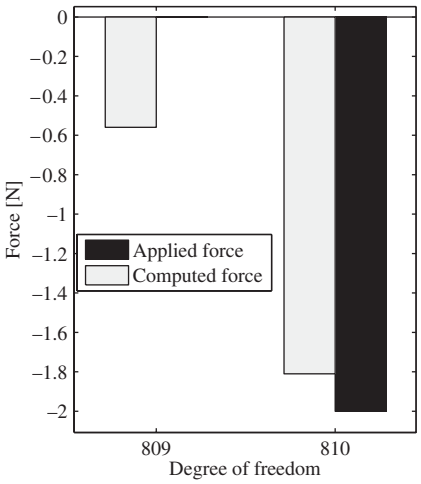

Figure 33. Force response with MMSF under 5%.

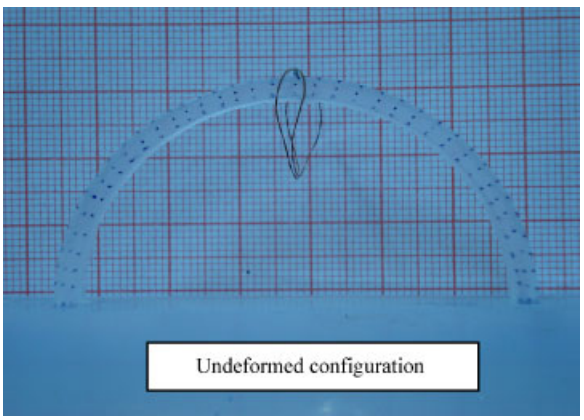

Figure 34. Undeformed configuration in the experiment.

The error in the estimated forces by DPIM is 1300.87% for 5% noise in the displacement data. However, MMSF brings the error in the estimated force to 29.55%, which gives the estimated force in the same order of magnitude as the expected force as shown in Figure 33. The error of 29.55% is high. This may be because the horizontal (i.e. axial) stiffness of the beam is 1600 times larger than the vertical (i.e. bending) stiffness. Such a case is known to be prone to increased error [1].

5.8. Example 8: experimental verification

Although the above numerical examples provided some insight into the methods, this last example is considered for validating the method with an experiment. We conducted the experiment on a silicone rubber arch beam as shown in Figure 34. It was vacuum-cast using a mould. The mould for this was made with a polypropylene sheet by using a computer numerically controlled (CNC)

DOI: 10.1002/nme

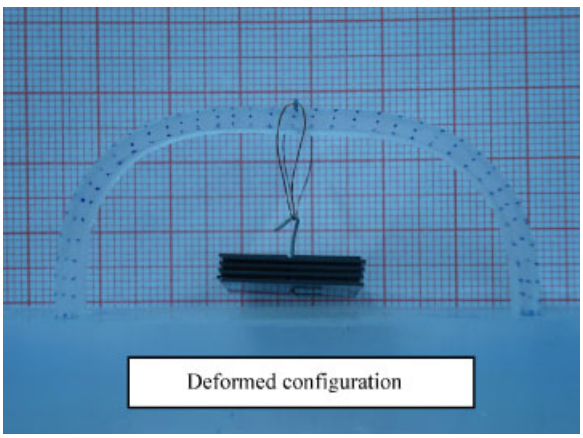

Figure 35. Deformed configuration in the experiment.

milling machine. This arch beam had an outer radius of 30 mm, an inner radius of 27.5 mm, and a thickness of 5 mm. Young's modulus was taken as 1.5 MPa and Poisson's ratio was taken as 0.48. The ends of the beam were fixed in a vice while a pre-determined point load is applied on the beam as shown in Figure 35. The images of the deformed and undeformed configurations were captured using a digital camera. The measured displacement data are given in Appendix A.3. Two meshes were considered with 4-noded and 9-noded elements. The load applied on the arch beam was 0.0745 N by hanging metallic pieces that we calibrated using a digital balance. The estimated force using MMSF was 0.1109 N with the 4-noded quad element and 0.075 N with the 9-noded quad element. Therefore, an error of 48.86% with the 4-noded element and an error of 1.04% with the 9-noded element were obtained. The larger error with 4-noded element than the 9-noded element is due to the stiff nature of the 4-noded element as is well known in the finite element analysis literature. Therefore, a 9-noded element is suitable for the practical problems in the force-sensing application. The low error obtained in this experiment validates the effectiveness of MMSF in practice.

6. CONCLUSION

Two methods are presented in this paper to solve the Cauchy's problem in elasticity. Although considerable literature exists on methods to solve this problem, almost all of them were limited to small displacements. Here, vision-based force-sensing required us to consider large displacements, rotations, and strains of an elastic body, which is a compliant grasping and manipulating tool. Our first method uses a pseudo-inverse technique to solve an over-constrained system of equations. We noted that this method, similar to the earlier methods, gives unacceptably large errors in forces due to high noise in the measured displacements. We reasoned that this is due to spurious forces that arise at locations where there should not be any forces. Hence, in our second method, we posed a minimization problem to suppress the spurious forces by optimally adjusting the measured displacements within the accuracy of the measurement technique. All numerical examples presented here underscore the importance of minimizing spurious forces. In fact, in Example 5.4, we showed

DOI: 10.1002/nme

that imposing smoothness on the force distribution does not prevent the spurious forces. Even though the second method performed well in most numerical examples, it gave a large error in Example 5.7. As noted in Section 5.7, this happens when there is a large difference in the displacements caused by a force acting in different directions at a point where forces are to be computed. Presently, we have only one example where this has happened. This, however, is not a serious practical limitation for vision-based force-sensing because the grasping/manipulating tool can be designed to avoid this situation. Arch beam considered in the experimental validation of the second method is an example of such an elastic body.

APPENDIX A

A.1. Computing the tangent stiffness matrix of an elastic body

In this section, for completeness of the paper and for immediate reference of the reader, we present the details of computing the reduced tangent stiffness matrix of an elastic body undergoing large displacements. We begin with the definition of the internal forces, $\mathbf{F}_{\text{int}}$, inside a 2D elastic body:

$$\mathbf{F}_{\text{int}} = \int_{\Omega} \mathbf{B}^{\mathrm{T}} \mathbf{S} \partial\Omega \tag{A1}$$

where $\mathbf{S}$ is the stress components in vector form and $\mathbf{B}$ is the incremented strain–displacement matrix. The material constitutive relationship, $\mathbf{D}$, which is assumed to be linear here for plane-stress condition, relates the stress, $\mathbf{S}$, and strain, $\mathbf{E}$:

$$\mathbf{S} = \mathbf{D}\mathbf{E} \tag{A2}$$

with

$$\mathbf{D} = \frac{Y}{1-v^2} \begin{pmatrix} 1 & v & 0 \\ v & 1 & 0 \\ 0 & 0 & 1-v \end{pmatrix} \tag{A3}$$

where Y is Young's modulus and v is Poisson's ratio.

The strain–displacement matrix, $\mathbf{B}$, relates the differential changes in the strain, $\mathbf{E}$, and the nodal displacement vector, $\mathbf{p}$:

$$\delta\mathbf{E} = \mathbf{B}\delta\mathbf{p} \tag{A4}$$

The nodal displacement vector consists of the x and y components of the displacement at all the nodes:

$$\mathbf{p} = \{u_1 \;\; v_1 \;\; u_2 \;\; v_2 \cdots\}^{\mathrm{T}} \tag{A5}$$

We use Green's strain as a measure for $\mathbf{E}$. This is defined as shown below with its linear and non-linear components:

$$\mathbf{E} = \mathbf{E}_{\text{l}} + \mathbf{E}_{\text{nl}} = \mathbf{E}_{\text{l}} + \tfrac{1}{2}\mathbf{A}\boldsymbol{\theta} = [\mathbf{H} + \tfrac{1}{2}\mathbf{A}]\boldsymbol{\theta} \tag{A6}$$

DOI: 10.1002/nme

where $\mathbf{A}$, $\boldsymbol{\theta}$, and $\mathbf{H}$ are as follows:

$$\mathbf{A}=\begin{pmatrix} \dfrac{\partial u}{\partial x} & 0 & \dfrac{\partial v}{\partial x} & 0 \\ 0 & \dfrac{\partial u}{\partial y} & 0 & \dfrac{\partial v}{\partial y} \\ \dfrac{\partial u}{\partial y} & \dfrac{\partial u}{\partial x} & \dfrac{\partial v}{\partial y} & \dfrac{\partial v}{\partial x} \end{pmatrix}, \quad \boldsymbol{\theta}=\begin{Bmatrix} \dfrac{\partial u}{\partial x} & \dfrac{\partial u}{\partial y} & \dfrac{\partial v}{\partial x} & \dfrac{\partial v}{\partial y} \end{Bmatrix}^{\mathrm{T}}, \quad \mathbf{H}=\begin{bmatrix} 1 & 0 & 0 & 0 \\ 0 & 0 & 0 & 1 \\ 0 & 1 & 1 & 0 \end{bmatrix} \tag{A7}$$

A differential change in $\mathbf{E}$ can be obtained as follows:

$$\delta\mathbf{E}=\delta\mathbf{E}_{\mathrm{l}}+\tfrac{1}{2}\mathbf{A}\delta\boldsymbol{\theta}+\tfrac{1}{2}\delta\mathbf{A}\boldsymbol{\theta}+\mathrm{O}(\delta\boldsymbol{\theta}^{\mathrm{T}}\delta\boldsymbol{\theta})=\delta\mathbf{E}_{\mathrm{l}}+\mathbf{A}\delta\boldsymbol{\theta}+\mathrm{O}(\delta\boldsymbol{\theta}^{\mathrm{T}}\delta\boldsymbol{\theta}) \tag{A8}$$

We note that

$$\begin{pmatrix} \dfrac{\partial u}{\partial x} & 0 & \dfrac{\partial v}{\partial x} & 0 \\ 0 & \dfrac{\partial u}{\partial y} & 0 & \dfrac{\partial v}{\partial y} \\ \dfrac{\partial u}{\partial y} & \dfrac{\partial u}{\partial x} & \dfrac{\partial v}{\partial y} & \dfrac{\partial v}{\partial x} \end{pmatrix} \begin{Bmatrix} \dfrac{\partial \delta u}{\partial x} \\ \dfrac{\partial \delta u}{\partial y} \\ \dfrac{\partial \delta v}{\partial x} \\ \dfrac{\partial \delta v}{\partial y} \end{Bmatrix} = \begin{pmatrix} \dfrac{\partial \delta u}{\partial x} & 0 & \dfrac{\partial \delta v}{\partial x} & 0 \\ 0 & \dfrac{\partial \delta u}{\partial y} & 0 & \dfrac{\partial \delta v}{\partial y} \\ \dfrac{\partial \delta u}{\partial y} & \dfrac{\partial \delta u}{\partial x} & \dfrac{\partial \delta v}{\partial y} & \dfrac{\partial \delta v}{\partial x} \end{pmatrix} \begin{Bmatrix} \dfrac{\partial u}{\partial x} \\ \dfrac{\partial u}{\partial y} \\ \dfrac{\partial v}{\partial x} \\ \dfrac{\partial v}{\partial y} \end{Bmatrix} \Rightarrow \delta\mathbf{A}\boldsymbol{\theta}=\mathbf{A}\delta\boldsymbol{\theta} \tag{A9}$$

By neglecting the second- and higher-order terms in Equation (A8), we can re-write it as

$$\delta\mathbf{E}=[\mathbf{H}+\mathbf{A}]\delta\boldsymbol{\theta} \tag{A10}$$

The x- and y-components of the displacements are now interpolated using shape functions and nodal displacement vector, $\mathbf{p}$:

$$\begin{aligned} u &= \sum_i N_i u_i \\ v &= \sum_i N_i v_i \end{aligned} \tag{A11}$$

where N_i's are the shape functions. This enables us to express $\boldsymbol{\theta}$ as follows:

$$\boldsymbol{\theta}=\mathbf{G}\mathbf{p} \tag{A12}$$

DOI: 10.1002/nme

where

$$\mathbf{G}=\begin{bmatrix} \dfrac{\partial N_1}{\partial x} & 0 & \dfrac{\partial N_2}{\partial x} & 0 & \cdots \\ \dfrac{\partial N_1}{\partial y} & 0 & \dfrac{\partial N_2}{\partial y} & 0 & \cdots \\ 0 & \dfrac{\partial N_1}{\partial x} & 0 & \dfrac{\partial N_2}{\partial x} & \cdots \\ 0 & \dfrac{\partial N_1}{\partial y} & 0 & \dfrac{\partial N_2}{\partial y} & \cdots \end{bmatrix} \tag{A13}$$

Noting that $\delta\boldsymbol{\theta}=\mathbf{G}\delta\mathbf{p}$, we can re-write Equation (11) as

$$\delta\mathbf{E}=[\mathbf{H}+\mathbf{A}]\mathbf{G}\delta\mathbf{p}=\mathbf{B}\delta\mathbf{p} \tag{A14}$$

leading to

$$\mathbf{B}=[\mathbf{H}+\mathbf{A}]\mathbf{G} \tag{A15}$$

We now consider the perturbation of $\mathbf{F}_{\text{int}}$ with respect to the nodal displacement vector, $\mathbf{p}$. This gives us the tangent stiffness matrix:

$$\delta\mathbf{F}_{\text{int}}=\int_{\Omega}(\mathbf{B}^{\mathrm{T}}(\delta\mathbf{S})+(\delta\mathbf{B})^{\mathrm{T}}\mathbf{S})\partial\Omega \tag{A16}$$

By substituting for $\delta\mathbf{S}$ and $\delta\mathbf{B}$, we obtain

$$\delta\mathbf{F}_{\text{int}}=\int_{\Omega}(\mathbf{B}^{\mathrm{T}}\mathbf{D}\mathbf{B}\delta\mathbf{p}+\mathbf{G}^{\mathrm{T}}\delta\mathbf{A}^{\mathrm{T}}\mathbf{S})\partial\Omega \tag{A17}$$

By defining $\hat{\mathbf{S}}$ as shown below, we can re-write $\delta\mathbf{A}^{\mathrm{T}}\mathbf{S}$ as $\hat{\mathbf{S}}\delta\boldsymbol{\theta}$:

$$\hat{\mathbf{S}}=\begin{bmatrix} S_{11} & S_{12} & 0 & 0 \\ S_{12} & S_{22} & 0 & 0 \\ 0 & 0 & S_{11} & S_{12} \\ 0 & 0 & S_{12} & S_{22} \end{bmatrix} \Rightarrow \delta\mathbf{A}^{\mathrm{T}}\mathbf{S}=\hat{\mathbf{S}}\delta\boldsymbol{\theta} \tag{A18}$$

Now, Equation (A17) takes the following form by virtue of Equation (13):

$$\begin{aligned}\delta\mathbf{F}_{\text{int}} &= \int_{\Omega}(\mathbf{B}^{\mathrm{T}}\mathbf{D}\mathbf{B}\delta\mathbf{U}+\mathbf{G}^{\mathrm{T}}\hat{\mathbf{S}}\delta\boldsymbol{\theta})\partial\Omega \\ &= \left[\int_{\Omega}(\mathbf{B}^{\mathrm{T}}\mathbf{D}\mathbf{B}+\mathbf{G}^{\mathrm{T}}\hat{\mathbf{S}}\mathbf{G})\partial\Omega\right]\delta\mathbf{p}=\mathbf{K}_{\mathrm{T}}\delta\mathbf{p}\end{aligned} \tag{A19}$$

DOI: 10.1002/nme

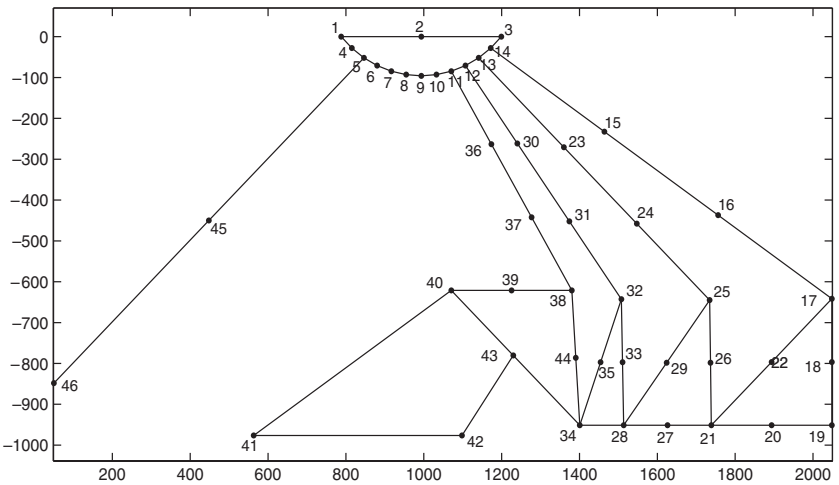

Figure A1. The geometry of the displacement-amplifying compliant mechanism.

Table AI. The geometric details of the displacement-amplifying compliant mechanism.

Element number	Head node	Tail node	Width of the beam (μm)	Element number	Head node	Tail node	Width of the beam (μm)
1	1	2	45	28	26	21	6
2	2	3	45	29	21	27	3
3	1	4	45	30	27	28	3
4	4	5	45	31	28	29	10.5
5	5	6	45	32	29	25	10.5
6	6	7	45	33	12	30	3
7	7	8	45	34	30	31	3
8	8	9	45	35	31	32	3
9	9	10	45	36	32	33	6
10	10	11	45	37	33	28	6
11	11	12	45	38	28	34	3
12	12	13	45	39	34	35	3
13	13	14	45	40	35	32	3
14	14	3	45	41	11	36	3
15	14	15	8	42	36	37	3
16	15	16	8	43	37	38	3
17	16	17	8	44	38	39	3
18	17	18	6	45	39	40	3
19	18	19	6	46	40	41	24
20	19	20	6	47	41	42	24
21	20	21	6	48	40	43	24
22	21	22	12	49	43	42	24
23	22	17	12	50	43	34	6
24	13	23	6	51	34	44	3
25	23	24	3	52	44	38	3
26	24	25	3	53	5	45	24
27	25	26	6	54	45	46	24

DOI: 10.1002/nme

where the tangent stiffness matrix, $\mathbf{K}_T$, relating the change in the nodal displacement vector and the change in the internal force vector is defined as follows with its linear and non-linear parts:

$$\mathbf{K}_T = \mathbf{K}_{Tl} + \mathbf{K}_{Tnl} = \int_\Omega (\mathbf{B}^T \mathbf{D}\mathbf{B} + \mathbf{G}^T \hat{\mathbf{S}}\mathbf{G})\, d\Omega \tag{A20}$$

For further details regarding internal force and tangent stiffness matrix refer [29] or any book on non-linear finite element methods. Similarly, co-rotational beam element formulation can also be found in [29]. The $\mathbf{K}_T$ shown in the main body of the paper is the reduced stiffness matrix wherein the specified zero displacements on Γ_{fixed} are applied.

A.2. The geometric details of the displacement-amplifying compliant mechanism

The geometric details of the displacement-amplifying compliant mechanism are given Figure A1 and Table AI.

A.3. Experimental data of the arch beam

All dimensions are in mm. Locations of the five points are indicated in Figure A2. The measured displacements in the arch beam experiment are given in Table AII.

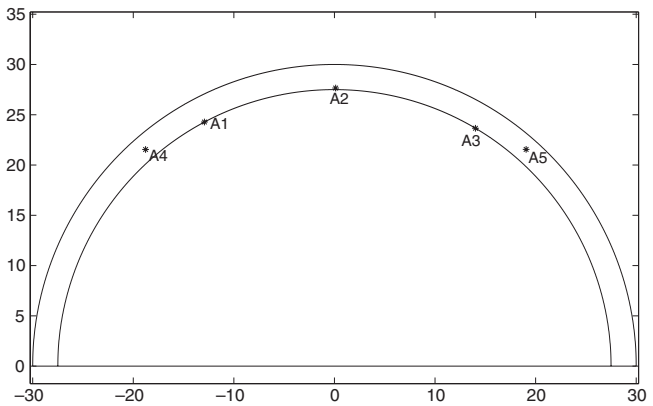

Figure A2. Geometry of the arch beam considered in Example 5.8.

Table AII. The measured displacements in the arch beam experiment.

Node	X-coordinate	Y-coordinate	Displacement along X (u)	Displacement along Y (v)
A1	−12.9270	24.2723	−0.89268	−1.04700
A2	0.1179	27.6574	−0.30179	−3.67037
A3	14.0205	23.6574	0.43160	−1.29579
A4	−18.7717	21.5476	−1.25654	0.21422
A5	19.0497	21.5542	0.71191	−0.27783

DOI: 10.1002/nme

ACKNOWLEDGEMENTS

The authors would like to thank Sudarshan Hedge for helpful discussions; Sridhar (CPDM) and G. Balaji for their help in making the beam using vacuum casting and its mould on a CNC machine; Nandan Maheswari for designing the gripper in Figure 1(a); Girish Krishnan for providing the geometry of the displacement-amplifying compliant mechanism; and Sivanagendra for providing geometric non-linear co-rotational beam element MATLAB code. The authors thank the department of Centre for Product Design and Manufacturing at the Indian Institute of Science, Bangalore, for providing vacuum casting and CNC machining facilities. This work is supported in part by the Swarnajayanthi fellowship of the Department of Science and Technology, Government of India, to the second author.

REFERENCES

1. Wang X, Ananthasuresh GK, Ostrowski JP. Vision-based sensing of forces in elastic objects. *Sensors and Actuators A*: *Physical* 2001; **94**(3):142–156.
2. Greminger MA, Nelson BJ. Vision-based forces measurement. *IEEE Transactions on Pattern Analysis and Machine Intelligence* 2004; **26**(3):290–298.
3. Kamiyama K, Vlack K, Mizota T, Kajimoto H, Kawakami N, Tachi S. Vision-based sensor for real time measuring of surface traction. *IEEE Computer Graphics and Applications* 2005; **25**(1):68–75.
4. Vendroux G, Knauss WG. Submicron deformation field measurements. Part 2. Improved digital image correlation. *Experimental Mechanics* 1998; **38**(2):86–92.
5. Charette PG, Hunter IW, Hunter PJ. Large deformation mechanical testing of biological membranes using speckle interferometry in transmission. I: experimental apparatus. *Applied Optics* 1997; **36**(10).
6. Zhang R, Shilo D, Ravichandran G, Bhattacharya K. Mechanical characterization of released thin films by contact loading. *ASME Journal of Applied Mechanics* 2006; **73**:730–736.
7. Schnur DS, Zabaras N. Finite element solution of two-dimensional inverse elastic problems using spatial smoothing. *International Journal for Numerical Methods in Engineering* 1990; **30**(1):57–75.
8. Bonnet M, Constantinescu A. Inverse problems in elasticity. *Inverse Problems* 2005; **21**:R1–R50.
9. Tikhonov AN, Arsenin VY. *Solution of Ill-posed Problems*. V.H. Winston: Washington, DC, 1977.
10. Belgacem FB. Why is the Cauchy problem severely ill-posed? *Inverse Problems* 2007; **23**:823–826.
11. Krishnan G, Ananthasuresh GK. An objective evaluation of displacement-amplifying compliant mechanisms for sensor applications. *CD-ROM Proceedings of the ASME International Design Engineering and Technical Conferences*, Philadelphia, U.S.A., 10–13 September 2006; Paper #DETC2006-99345 (Also to appear in the *Journal of Mechanical Design* 2008).
12. Oda J, Moto S. On inverse analytical technique to obtain contact stress distributions-technique using measurement values with errors (in Japanese but with an abstract in English). *Transactions of the Japan Society of Mechanical Engineers*, *Series A* 1980; **55**:827–877.
13. Maniatty A, Zabaras N, Stelson K. Finite-element analysis of some inverse elasticity problems. *Journal of Engineering Mechanics* (ASCE) 1989; **115**(11):1303–1317.
14. Zabaras N, Morellas V, Schnur D. Spatially regularized solution of inverse elasticity problems using the BEM. *Communications in Applied Numerical Methods* 1989; **5**(3):547–553.
15. Maniatty AM, Zabaras NJ. Investigation of regularization parameters and error estimating in inverse elasticity problems. *International Journal for Numerical Methods in Engineering* 1994; **37**(6):1039–1052.
16. Bezerra LM, Saigal S. Inverse boundary traction reconstruction with the BEM. *International Journal of Solids and Structures* 1995; **32**(10):1417–1431.
17. Martin TJ, Halderman JD, Dulikravich GS. An inverse method to finding unknown surface tractions and deformations in elastostatics. *Computers and Structures* 1995; **56**(5):825–835.
18. Zhang F, Kassab AJ, Nicholson DW. A 3-D traction reconstruction method using BEM and internal strain data. *AIAA/ASME/ASCE/AHS/ASC Structures*, *Structural Dynamics*, *and Materials Conference and Exhibit*, *38th*, *and AIAA/ASME/AHS Adaptive Structures Forum*, Kissimmee, FL, U.S.A., 7–10 April 1997; 1873–1883.
19. Lu S, Rizzo FJ. A boundary element strategy for elastostatic inverse problems involving uncertain boundary conditions. *International Journal for Numerical Methods in Engineering* 1999; **46**:957–972.
20. Turco E. An effective algorithm for reconstructing boundary conditions in elastic solids. *Computer Methods in Applied Mechanics and Engineering* 2001; **190**(29–30):3819–3829.

DOI: 10.1002/nme

21. Nakagiri S, Suzuki K. Finite element interval analysis of external loads identified by displacement input with uncertainty. *Computer Methods in Applied Mechanics and Engineering* 1999; **168**:63–72.
22. Turco E. Is the statistical approach suitable for identifying actions on structures? *Computers and Structures* 2005; **83**:2112–2120.
23. Marine L. A meshless method for solving the Cauchy problem three-dimensional elastostatics. *Computers and Mathematics with Applications* 2005; **50**:73–92.
24. Kozlov VA, Maz'ya VG, Fomin AV. An iterative method for solving the Cauchy problem for elliptic equations. *Computational Mathematics and Mathematical Physics* 1991; **31**(1):45–52.
25. Baranger TN, Andrieux A. An optimization approach for the Cauchy problem in linear elasticity. *Structural and Multidisciplinary Optimization* 2008; **35**:141–152.
26. Belgacem FB, Feikh HE. On Cauchy's problem: I. A variational Steklov–Poincaré theory. *Inverse Problems* 2005; **21**:1915–1936.
27. Azaïez M, Belgacem FB, Fekih HE. On Cauchy's problem: II. Completion, regularization and approximation. *Inverse Problems* 2006; **22**:1307–1336.
28. Howell LL. *Compliant Mechanisms*. Wiley: New York, 2001.
29. Crisfield MA. *Non-Linear Finite Element Analysis of Solids and Structures*. Wiley: New York, 1997.

DOI: 10.1002/nme